DETERMINING DENSITIES IN DIFFUSE MOLECULAR CLOUDS VIA CO ABSORPTION

Trevor Picard
Department of Astronomy, University of Michigan, Ann Arbor, MI 48109, USA

ABSTRACT

One parameter that is important to interstellar chemistry is the density of H_2, but direct density measurement is impossible. We must therefore rely on methods of estimation based on the observable effects that H_2 density has on other molecules. One such effect is the excitation of CO through collisions with H_2, which is imprinted in the relative populations between CO rotational levels. Spectroscopic observations were made along 17 sight lines targeting ro-vibrational transitions out of the $0 \leq J \leq 6$ levels in the fundamental band of CO. These absorption features were analyzed to determine level-specific CO column densities, allowing us to express the relative populations between adjacent energy levels as excitation temperatures. By utilizing the analysis of Goldsmith (2013), which relates H_2 density to CO excitation temperatures, we inferred upper and lower limits on the H_2 density in several clouds. Many of our density results ($n \approx 10^2 - 10^4$ cm^{-3}) exceed those found by the Goldsmith (2013) sample, suggesting sight lines probing densities beyond typical diffuse molecular clouds ($n \gtrsim 10^3$ cm^{-3}). We also see a trend for individual sight lines where the inferred density increases when determined from higher J-level pairs. We discuss these findings and the future applicability of observations of CO in the infrared for constraining interstellar gas densities.

Keywords: ISM: clouds, molecules

1. INTRODUCTION

Interstellar chemistry is largely controlled by the density of H_2, which is the most abundant molecule in the universe. Properties like volume density ($n(H_2)$) are notoriously difficult to determine in the interstellar medium (ISM), owing to the fact that density is not directly measurable. The study of homonuclear molecules like H_2 in the ISM is hindered by their symmetry, which prevents H_2 from possessing a permanent dipole moment. Electric quadrupole transitions are several orders of magnitude weaker than dipole transitions, so H_2 emission is difficult to observe under typical diffuse molecular cloud conditions.

The influence that H_2 has on observable molecules like CO, the second most abundant molecule in the ISM, allows us to study its properties indirectly. For instance, populations in several of the lowest rotational energy states ($J \leq 3$) of CO have been shown to be useful for tracing the gas density in diffuse molecular clouds (Goldsmith 2013). This is because collisions between H_2 and CO molecules result in excitation or de-excitation of rotational quantum levels of CO. As a result, we can gain insight into gas density through collisional excitation, provided that CO column densities in individual J-levels can be determined.

Previous studies have determined CO column densities by observing diffuse molecular clouds in the UV, which probe the electronic transitions of CO (e.g., Sheffer et al. 2008; Sonnentrucker et al. 2007). Such observations are useful because they allow simultaneous measurements of multiple quantum transitions, which are sensitive to the J-levels of CO in the observed cloud. Determination of CO column densities is not limited to observations in the UV; ro-vibrational transitions in the fundamental band of CO ($v = 1 - 0$) form IR absorption lines when viewed against bright background sources, offering a method of observing the transitions in cold, diffuse clouds. Probing these IR transitions would then allow us to determine level-specific CO column densities (N(CO)).

The relative populations of CO J-levels in diffuse clouds, which we express as excitation temperatures (T^{ex}), are related to H_2 density by current theoretical models (Goldsmith 2013). We can constrain $n(H_2)$ in diffuse molecular clouds by utilizing these models and analytical methods. Current studies relating CO collisional excitation to H_2 densities are sparse and mainly limited to quoting upper $n(H_2)$ limits, so we seek to further constrain interstellar gas densities and include clouds that sample denser material ($n(H_2) \gtrsim 10^3$ cm^{-3}). These investigations should provide insight into the utility of observing CO transitions in the IR for constraining interstellar gas densities.

2. OBSERVATIONS

The observations utilized in this study were made using multiple telescopes and instruments, which are summarized in Table 1. Most of the sight lines were observed between April 2, 2011 and April 2, 2012 using the Cryogenic High-resolution Infrared Echelle Spectrograph (CRIRES; Käufl et al. 2004) at the Very Large Telescope. Observations were performed in service mode, and CRIRES was used with its 0.″2 slit to provide a resolving power (resolution) of about 100,000 (3 km s^{-1}). A reference wavelength of 4.681 μm (the central wavelength of the third detector) set the wavelength ranges on detectors 1 through 4 to be 4.6073–4.6322 μm, 4.6392–4.6632 μm, 4.6695–4.6925 μm, and 4.6984–4.7204 μm, respectively. The adaptive optics system was utilized, and spectra were obtained in an ABBA pattern with 10″ between the two nod positions and $\pm 3''$ jitter width.

Further observations were made at the United Kingdom Infrared Telescope (UKIRT), utilizing the Cooled Grating Spectrometer 4 (CGS4; Mountain et al. 1990). CGS4 was used with its echelle grating, 0.″6 wide slit, and long camera to provide a resolving power (resolution) of about 40,000 (8 km s^{-1}). A circular variable order-blocking filter was used to select the order containing the $R(0)$ through $R(3)$ transitions of CO. The telescope was nodded 7.13 arcsec along the slit, and the 3×2 sampling mode was employed. Further details on the reduction of

CGS4 data leading to wavelength calibrated spectra can be found in Indriolo (2011).

Observations at the Infrared Telescope Facility (IRTF) were made using CSHELL (Greene et al. 1993), with its 0.″5 slit providing a resolving power (resolution) of about 43,000 (7 km s^{-1}). A circular variable filter was used to select the order containing the $R(0)$ and $R(1)$ transitions of CO, and the telescope was nodded by about 15 arcsec along the slit.

3. DATA PROCESSING

All of the CRIRES data were reduced through the standard data pipeline provided by the European Southern Observatory (ESO). The CRIRES pipeline corrects for the non-linearity of the detectors, provides flat-fielding, corrects for bad pixels, subtracts image pairs to remove sky emission, and then combines spectral images by averaging.

3.1. *IRAF Aperture Fitting*

CRIRES has four detectors, each with an aperture to be extracted using IRAF. We ran the aperture extraction for each sight line in interactive mode, noticing that sometimes points with a strong absorption feature skew the aperture fitting function, forcing us to manually delete those points to obtain a reasonable low-order fit.

We also inspected the extracted spectra of science targets and their corresponding telluric standard stars in IRAF. Noise spikes and other remaining "bad" pixels often remained in the extracted spectra, which were removed via linear interpolation. Most noise spikes are not located within the narrow wavelength ranges of the CO absorption features, and thus they don't appreciably affect the final numerical analysis. Removing noise spikes gives the final plots more clarity and prevents true absorption features from being overlooked.

3.2. *IGOR Pro Calibration & Processing*

Extracted science spectra were imported into IGOR Pro for calibration and processing. We first divided the science targets by their telluric standard stars. The standard spectra can be scaled during the division process, allowing the best removal of atmospheric lines. Next we followed the wavelength calibration procedure outlined in McCall (2001), using atmospheric absorption features at known wavelengths as calibration markers. The pixel values in the dispersion direction were transformed into wavelength space by a second order polynomial fit (the calibration is accurate to within ∼1 km s^{-1}).

Many spectra showed significant deviation from continuum level following the division by their standard stars. Intense atmospheric CO absorption is to blame for these remaining spectral artifacts, which can be eliminated via division by a moving average (with high spectral resolution CO absorption features purposely excluded from the moving average).

3.3. *CO Detections*

CO was detected in 11 of the 17 observed sight lines. The reduced, baseline corrected spectra are shown in Figures 1 and 2, plotted along with the atmospheric spectrum. Each spectrum's continuum level is arbitrarily shifted for comparison. Nearly all of the clouds with CO detections have a single velocity component. The notable exception is WR 105, which has an additional velocity component, as shown in Figure 3. The cloud component that is receding at ∼5 km s^{-1} in the LSR frame has significantly deeper absorption features than its more quickly receding companion at ∼17 km s^{-1}. We detected CO transitions in the former component in states up to $J = 6$, while no CO was detected beyond the $J = 3$ states for the latter component.

The other six sight lines in Table 1 showed no statistically significant CO features following data reduction and baseline correction. Non-detections indicate either low CO column densities or unfavorable Doppler shifts of the lines, causing them to be obscured by atmospheric absorption. In the case of HD 169454, the atmospheric interference of the $R(0)$ transition prevented us from obtaining a meaningful rotation temperature out of the analysis.

4. ANALYSIS

The calibrated, baseline corrected spectra were fit with Gaussian functions, allowing us to calculate various absorption line parameters, including the Local Standard of Rest (LSR) velocity, line width, and equivalent width (W_λ). We estimate the uncertainties in equivalent width based on the standard deviation of the noise level on the continuum, given as

$$\sigma(W_\lambda) = \lambda_{pix}\sigma_c\sqrt{\mathcal{N}}, \tag{1}$$

where λ_{pix} is the wavelength step per pixel, σ_c is the continuum level standard deviation near the absorption feature, and $\mathcal{N}$ is the number of pixels that the absorption line covers. We measured σ_c based on the noise surrounding each absorption feature, since the deviations from the continuum level sometimes changes appreciably within a single spectrum.

The absorption line parameters for CO detections are summarized in Table 2. We found that uncertainties in W_λ are typically ∼10% of the observed values, which is reasonable given the typical detection's signal-to-noise ratio. No sensible Gaussian fit could be obtained for the $R(0)$ transition of HD 169454, primarily due to interference by the atmospheric CO absorption feature at 4.65748μm.

4.1. *CO Column Densities*

Each absorption line's equivalent width is related to the column density of CO. In diffuse molecular clouds CO absorption lines are relatively weak and are expected to be optically thin, so we use the column density equation applicable in the optically thin limit, given by

$$N_l = W_\lambda \frac{g_l}{g_u}\frac{8\pi c}{A_{ul}\lambda^4}, \tag{2}$$

where N_l is the column density in the lower state associated with the observed transition, g_l and g_u are statistical weights of the lower and upper states, c is the speed of light, A_{ul} is the spontaneous emission coefficient, and

λ is the transition wavelength. Uncertainty in CO column density ($\sigma(N_l)$) is calculated simply by replacing W_λ with $\sigma(W_\lambda)$ in Equation (2).

The column densities in each J-state are also shown in Table 2. For non-detections it is impossible to know whether N(CO) values in the clouds are too low to analyze, or if Doppler shifts obfuscate otherwise present absorption features. Without statistically significant CO absorption features collisional excitation cannot be analyzed, and therefore cloud densities cannot be constrained using our method.

4.2. *Optical Depth Effects*

Our assumption of optically thin transitions is not valid for sight lines with absorption features deeper than ~50%. For optically thick lines we know that W_λ alone is a poor indicator of N(CO). The equivalent width for optically thick absorption is instead governed by

$$\frac{W_\lambda}{\lambda} = \frac{2bF(\tau)}{c}, \tag{3}$$

where τ is the optical depth, b is the Doppler parameter, and $F(\tau)$ is defined by the integral

$$F(\tau) = \int_0^\infty [1 - \exp(-\tau \exp(-x^2))]dx. \tag{4}$$

The dependence of $F(\tau)$ on optical depth can be determined by numerically integrating Equation (4) over a large range of τ. Adopting a particular value of b in conjunction with measured values of W_λ and λ, we can use Equation (3) to solve for the corresponding $F(\tau)$. Our observed $F(\tau)$ can then be compared with the numerical solution to Equation (4), giving us a best fit value for τ for the chosen Doppler parameter. With a known, non-negligible value of τ, we can use the equation

$$N_l = \frac{8\pi^{3/2}\tau b}{A_{ul}\lambda^4}\frac{g_l}{g_u} \tag{5}$$

to compute the lower state's column density in the saturated regime.

Since column density is a function of which b value is chosen, iterating over a range of b should reveal the desired dependence. Typical values of b are between 0 and 10 km/s, so this is the iteration range we use (in steps of 0.1 km/s). Each transition will have its own dependence of column density on b, although all transitions asymptotically approach their column densities in the optically thin limit (see Table 2) as $b \to \infty$. We are interested in where the two curves of the same J-state intersect, which reveals the column density that is consistent with both the $R(J)$ and $P(J)$ transitions, along with its associated b value.

Values of N_l calculated in the optically thin limit often disagreed between $R(J)$ and $P(J)$ transitions probing the same rotational state, with $R(J)$ transitions systematically underestimating N_J values (see Table 2). Curve of growth analysis was only moderately effective in reducing these discrepancies, in many cases resulting in relatively large uncertainties in N(CO) and T^{ex}. HD 78344 is one of a few sight lines with absorption features deeper than ~50%, resulting in the significant CO column density disagreement between $P(J)$ and $R(J)$ transitions probing the same rotational state. We had little success with the sight lines in Figure 1 containing the deepest features, specifically HD 78344. The $J = 2$ transitions converged on a column density of $N_J = 5.5 \times 10^{15}\text{cm}^{-2}$, corresponding to a Doppler parameter of $b = 0.84$ km/s. However, the $J = 0$ column density associated with this Doppler parameter is several orders of magnitude greater, suggesting that it is wildly inaccurate. In the cases where COG analysis was unsuccessful we averaged the $P(J)$ and $R(J)$ column densities to obtain a single value for each rotational level.

4.3. *Excitation Temperatures*

The relative populations between rotational states can be expressed as

$$\frac{N_u}{N_l} = \frac{g_u}{g_l}\exp(-\frac{\Delta E}{T^{ex}_{ul}}), \tag{6}$$

where T^{ex} is the excitation temperature and ΔE is the energy difference between the states in units of temperature (K). Information about the relative populations between CO rotational states is encoded within T^{ex}. Solving for this quantity gives

$$T^{ex}_{ul} = -\frac{\Delta E}{\ln\left[\frac{N_u g_l}{N_l g_u}\right]}. \tag{7}$$

The behavior of T^{ex} as a function of total CO column density (N_{tot}(CO)) is of particular interest. Figure 4 shows how T^{ex} varies over a wide range of total CO column densities, which are obtained simply by summing over level-specific N(CO) values. This study obtained data clustered around $N_{tot}(\text{CO}) \sim 10^{16}$ cm^{-2}, so to increase our sample size and range of column densities we included IR data from McCall et al. (2002) and UV data from Goldsmith (2013), which vary from $N_{tot}(\text{CO}) \sim 10^{12} - 10^{16}$ cm^{-2}. We find that T^{ex} increases with N_{tot}(CO).

4.4. *Density Modeling*

Once we have obtained excitation temperatures, we must relate the information about the relative populations to H_2 densities. This is accomplished by using a computer program called Radex (van der Tak et al. 2007), which models the radiative transfer environment within interstellar clouds with uniform density. Our first CO collisional excitation model relating T^{ex} to $n(H_2)$ is shown in Figure 5. The model uses the collision rate coefficients from Yang et al. (2010), which can be found in the LAMDA database. We take into account the different H_2 species as collision partners, adopting a standard ortho-to-para H_2 ratio of 3. As shown by Goldsmith (2013), varying the ortho-to-para ratio for H_2 from 1 to 3 does not make a significant difference in T^{ex} for a given value of $n(H_2)$. We also assume a kinetic temperature of $T_k = 100$K, which is roughly the average temperature in diffuse molecular clouds (Savage et al. 1977). Goldsmith (2013) showed that T^{ex} is relatively insensitive to choices of kinetic temperature in the range $50\text{K} \leq T_k \leq 150\text{K}$ at low densities and transitions.

The model is further simplified due to various assumptions that we have made about the observed clouds. For instance, the total CO column density is assumed to be fixed at $N_{tot}(\mathrm{CO}) = 10^{14}$ cm^{-2}, allowing us to produce a model that is consistent with the optically thin regime ($\tau_{max} \approx 0.8$). Optical depth and radiative trapping affected the results marginally for the 1–0 line at this value of $N_{tot}(\mathrm{CO})$, suggesting that our model is valid in the limit of optically thin transitions.

Excitation temperatures and minimum/maximum estimates of H_2 number densities are given in Table 3. Most inferred densities ($n \approx 10^2 - 10^4$ cm^{-3}) are near the upper density limit of diffuse molecular clouds ($n \sim 10^3$ cm^{-3}), exceeding the Goldsmith (2013) sample. $n(H_2)$ estimates increase when determined from higher J-level pairs, possibly indicating absorption lines probing the edges of a molecular cloud. This result is consistent with the findings of Goldsmith (2013), specifically that the inclusion of $J = 2-1$ and $J = 3-2$ transitions tends to detect clouds, or regions within clouds, of appreciably higher density. Sight lines with larger $N_{tot}(\mathrm{CO})$ values appear to contain denser gas, as shown in Figure 6.

5. DISCUSSION

Our sample contains sight lines with higher CO column densities than those found by Goldsmith (2013), as shown in Figures 4 and 6. Typical diffuse clouds are $\lesssim 10$ pc in diameter, and the clouds in our sample are located at distances $\lesssim 2$ kpc, which offers a plausible explanation for the observed trends. Since nearly all sight lines have a single velocity component, we assume that each sight line (with the exception of WR 105) contains a single coherent cloud that is likely confined to a relatively small distance range. These general assumptions suggest that the vast majority of CO molecules are located within the observed cloud as opposed to other distances along the line of sight. It then follows that CO's collision partner (H_2) must be concentrated within the cloud as well. The relative abundance of CO with respect to H_2 increases at higher densities (Snow & McCall 2006), so a higher value of $N(\mathrm{CO})$ indicates a higher cloud density, i.e. a higher value of $n(H_2)$. This is precisely the trend observed in Figure 6. Furthermore, the aforementioned assumptions explain the similar trend seen in Figure 4. As CO column density rises, collisional excitation within the observed cloud will become the dominant mechanism in determining the relative populations between rotational states, simply because collisions between molecules are more probable in denser clouds. More frequent collisions would cause excitation temperatures to approach the kinetic temperature of the cloud. Thus, we expect T^{ex} to increase with $N(\mathrm{CO})$, which precisely matches the trend observed in Figure 4.

Another important result in Figure 6 is the clear discrepancy between $n(H_2)$ values when determined from different J-level pairs. Higher transitions seem to probe denser regions of a cloud, a result observed first by Goldsmith (2013), albeit with less clarity due to lower CO column densities. The sight lines from this study probe denser regions than the Goldsmith (2013) sample, where higher J-levels are more likely to be occupied and detectable. If we drop the simplistic assumption that the observed clouds have uniform densities, we discover a plausible explanation for this trend. The center of a molecular cloud is certainly more dense than the edges, and therefore we expect to detect transitions involving higher J-levels at the cloud's center. In contrast, Cosmic Microwave Background Radiation (CMBR; a blackbody at 2.73 K) is capable of exciting the $J = 1$ level of CO (5.5 K above the ground state) throughout the entirety of the cloud. The $1 - 0$ relative population yields a density averaged across the entire cloud, while the $3 - 2$ relative population probes only the inner regions, with the $2 - 1$ relative population yielding densities somewhere in between. This scenario is consistent with Figure 6 and provides a satisfactory explanation for the higher $n(H_2)$ estimates when determined from higher J-level pairs.

6. SUMMARY & FUTURE STUDIES

In this study we targeted ro-vibrational transitions out of the $0 \leq J \leq 6$ levels in the fundamental band of CO. Following data reduction, we determined that 11 of the 17 observed sight lines contained CO absorption lines. We analyzed the observed transitions to calculate level-specific column densities in the optically thin limit. While optical depth effects ended up being important in several sight lines, curve of growth analysis was ineffective in reducing the observed disparities in $N_J(\mathrm{CO})$ between $R(J)$ and $P(J)$ transitions into agreement within calculated uncertainties. This study obtained data clustered around $N_{tot}(\mathrm{CO}) \sim 10^{16}$ cm^{-2}, significantly higher on average than the sight lines observed by McCall et al. (2002) and Goldsmith (2013). Expressing the relative populations between adjacent rotational states of CO as excitation temperatures, we found that T^{ex} values approach the kinetic temperature of the cloud as $N_{tot}(\mathrm{CO})$ increases. This trend is explained by the increased importance of collisional excitation at high CO column densities.

We also used Radex (van der Tak et al. 2007) to model the radiative transfer environment in diffuse molecular clouds, providing us with a relationship between T^{ex} and H_2 density. With our calculated excitation temperatures and uncertainties, we could then put constraints on H_2 densities within the clouds we observed. Of the 39 detected transitions, 35 probe significantly denser material than the average value obtained by the Goldsmith (2013) study ($\langle n_{mid} \rangle = 94$ cm^{-3}). This is precisely what is expected given the large CO column densities in our sight lines. We found that $n(H_2)$ estimates increase when determined from higher J-level pairs, a trend that can be explained if we assume that the clouds we see are inhomogeneous. Higher J-level transitions would then probe the denser centers of the clouds, while lower J-level transitions would probe the entire cloud, including the more diffuse edges.

Our current analysis makes several simplifying assumptions, giving us a model that is not necessarily valid in general. We assumed that the clouds in our sight lines have uniform densities, a single kinetic temperature, and optically thin CO transitions. In future studies we plan to relax these assumptions, resulting in models with more general applicability. For instance, we plan to create a grid of Radex models, allowing T^k to vary with $n(H_2)$

as a free parameter. Variations in kinetic temperature will affect the results appreciably for the relatively dense regions probed in this study. In addition, we will use our calculated values of total CO column density as the input values for $N(\mathrm{CO})$ rather than assuming a value corresponding to the optically thin limit. Future attempts to obtain best fit models that account for these complications are certainly worthwhile, and also will not require excitation temperatures to express the relative populations between rotational states of CO. We believe that this analysis has a high potential of future applicability for determining densities in diffuse molecular clouds. Additionally, it reveals density inhomogeneities in sight lines with relatively high CO column densities, where higher rotational states are occupied and detectable.

I thank Nick Indriolo for his advice, mentorship, and careful scrutiny of my work, which extended from data reduction to interpretation of results. I also thank Paul Goldsmith for providing the theoretical framework upon which this study is based. Observations were made with ESO Telescopes at the La Silla Paranal Observatory under programme IDs 087.D-0066 and 088.D-0074. When the data reported here were acquired, UKIRT was operated by the Joint Astronomy Centre on behalf of the Science and Technology Facilities Council of the U.K.

REFERENCES

Goldsmith, P. F. 2013, ApJ, 774, 134
Greene, T. P., Tokunaga, A. T., Toomey, D. W., & Carr, J. B. 1993, in Proc. SPIE, Vol. 1946, Infrared Detectors and Instrumentation, ed. A. M. Fowler, 313–324
Indriolo, N. 2011, PhD thesis, University of Illinois
Käufl, H., Ballester, P., Biereichel, P., et al. 2004, Proc. SPIE, 5492, 1218
Lord, S. D. 1992, A new software tool for computing Earth's atmospheric transmission of near- and far-infrared radiation, Tech. rep.
McCall, B. J. 2001, PhD thesis, The University of Chicago
McCall, B. J., Hinkle, K. H., Geballe, T. R., et al. 2002, ApJ, 567, 391
Mountain, C. M., Robertson, D. J., Lee, T. J., & Wade, R. 1990, Proc. SPIE, 1235, 25
Savage, B. D., Bohlin, R. C., Drake, J. F., & Budich, W. 1977, ApJ, 216, 291
Sheffer, Y., Rogers, M., Federman, S. R., et al. 2008, ApJ, 687, 1075
Snow, T. P., & McCall, B. J. 2006, ARA&A, 44, 367
Sonnentrucker, P., Welty, D. E., Thorburn, J. A., & York, D. G. 2007, ApJS, 168, 58
van der Tak, F. F. S., Black, J. H., Schöier, F. L., Jansen, D. J., & van Dishoeck, E. F. 2007, A&A, 468, 627
Yang, B., Stancil, P. C., Balakrishnan, N., & Forrey, R. C. 2010, ApJ, 718, 1062

Table 1
Science Targets

Source	Date	Telescope	Instrument	Exposure Time (s)
HD 147889	2008 May 16	IRTF	CSHELL	2400
HD 169454	2008 May 16	IRTF	CSHELL	2040
NGC 2024 IRS 1	2008 Jan 25	UKIRT	CGS4	1920
HD 29647	2008 Jan 25	UKIRT	CGS4	1440
HD 168625	2007 Jul 3	UKIRT	CGS4	1440
HD 229059	2001 May 28	UKIRT	CGS4	1152
CD -23 13793	2011 Apr 2	VLT	CRIRES	960
HD 313599	2011 May 10	VLT	CRIRES	2040
WR 105	2011 May 17	VLT	CRIRES	320
HD 74194	2012 Mar 13	VLT	CRIRES	2040
HD 74194	2012 Mar 23	VLT	CRIRES	2040
HD 70583	2012 Apr 1	VLT	CRIRES	320
HD 72014	2012 Apr 1	VLT	CRIRES	720
HD 75149	2012 Apr 1	VLT	CRIRES	320
HD 75860	2012 Apr 1	VLT	CRIRES	320
CD -46 4786	2012 Apr 1	VLT	CRIRES	2040
HD 78344	2012 Apr 1	VLT	CRIRES	1200
HD 75211	2012 Apr 2	VLT	CRIRES	2040

Table 2
Absorption Line Parameters

Sight Line	Transition	$v_{\rm LSR}$ (km s^{-1})	FWHM (km s^{-1})	W_λ (10^{-5} μm)	N_J (10^{15} cm^{-2})
HD 313599	$R(0)$	12.9	12.2	3.80±0.47	1.74±0.21
	$R(1)$	11.5	4.4	1.48±0.20	1.01±0.14
	$P(1)$	10.9	4.1	1.20±0.20	1.65±0.28
	$R(2)$	11.9	5.2	1.69±0.32	1.29±0.24
	$P(2)$	11.5	4.5	1.36±0.29	1.55±0.13
HD 70583	$R(0)$	18.4	2.9	1.69±0.06	0.77±0.03
	$R(1)$	18.1	3.4	1.74±0.08	1.20±0.05
	$P(1)$	19.2	3.4	1.22±0.08	1.67±0.11
	$R(2)$	17.8	3.0	1.04±0.05	0.80±0.04
	$P(2)$	18.1	2.5	0.73±0.03	0.83±0.03
HD 75149	$R(0)$	6.0	8.1	0.86±0.08	0.39±0.04
	$R(1)$	3.8	6.4	0.28±0.05	0.19±0.04
CD-46 4786	$R(0)$	7.6	4.5	6.35±0.17	2.90±0.08
	$R(1)$	7.6	4.6	5.45±0.17	3.74±0.12
	$P(1)$	8.7	3.6	4.05±0.22	5.55±0.10
	$R(2)$	8.3	3.2	2.36±0.12	1.81±0.09
	$P(2)$	9.1	2.7	2.00±0.07	2.28±0.03
HD 78344	$R(0)$	4.9	4.7	9.30±0.11	4.26±0.05
	$R(1)$	4.9	4.4	7.82±0.09	5.37±0.06
	$P(1)$	3.3	4.6	7.28±0.22	9.96±0.10
	$R(2)$	4.4	3.9	3.10±0.08	2.37±0.06
	$P(2)$	5.5	4.1	2.60±0.14	2.96±0.07
HD 75211	$R(0)$	2.4	3.3	1.43±0.07	0.66±0.03
	$R(1)$	1.7	2.7	0.85±0.08	0.59±0.05
HD 169454	$R(1)$	4.1	8.1	2.57±0.33	1.76±0.23
NGC2024 IRS 1	$R(0)$	13.0	8.5	8.10±1.95	3.70±0.89
	$R(1)$	7.0	11.2	11.32±2.00	7.78±1.37
	$R(2)$	10.6	7.2	8.13±1.33	6.21±1.02
	$R(3)$	8.7	7.0	9.45±1.86	7.60±1.50
HD 229059	$R(0)$	3.1	10.2	5.48±0.70	2.51±0.32
	$R(1)$	3.6	6.4	2.97±0.42	2.04±0.29
	$R(2)$	5.0	6.2	1.11±0.34	0.85±0.26
HD 29647	$R(0)$	8.2	8.5	4.96±1.05	2.27±0.48
	$R(1)$	4.1	7.9	6.12±1.08	4.20±0.74
	$R(2)$	5.6	7.0	5.58±0.92	4.27±0.70
	$R(3)$	4.1	8.2	4.44±0.79	3.57±0.63
WR 105	$R(0)$	16.7	3.5	1.88±0.16	0.86±0.07
		5.2	4.2	6.14±0.19	2.81±0.09
	$R(1)$	17.1	2.9	1.89±0.10	1.30±0.07
		5.5	4.3	6.04±0.13	4.15±0.09
	$P(1)$	16.8	2.7	1.05±0.13	1.44±0.17
		4.7	3.8	5.03±0.15	6.88±0.21
	$R(2)$	16.1	2.6	1.07±0.15	0.82±0.12
		4.5	4.1	5.29±0.19	4.04±0.15
	$P(2)$	16.4	3.0	0.92±0.10	1.05±0.12
		4.7	3.9	4.94±0.12	5.63±0.13
	$P(3)$	18.4	5.5	0.71±0.15	0.76±0.16
		5.5	4.1	4.30±0.12	4.56±0.12
	$R(4)$	6.1	4.5	1.88±0.07	1.56±0.06
	$P(4)$	5.4	4.3	1.64±0.27	1.68±0.21
	$R(5)$	6.6	3.4	0.40±0.05	0.33±0.04
	$P(5)$	6.3	4.0	0.59±0.08	0.59±0.07
	$R(6)$	7.0	3.2	0.25±0.06	0.22±0.05

Note. — Columns 3, 4, 5, and 6 are the gas velocities in the local standard of rest frame, the line full widths at half maximum (FWHM = $2\sigma_v\sqrt{2\ln 2}$, where σ_v is the velocity dispersion), equivalent widths, and CO column densities in the optically thin limit, respectively.

Table 3
CO Column Densities, Excitation Temperatures, & H_2 Density Constraints

Sight Line	N_{tot}(CO) (10^{15} cm^{-2})	T_{10}^{ex} (K)	n_{min} (cm^{-3})	n_{max} (cm^{-3})	T_{21}^{ex} (K)	n_{min} (cm^{-3})	n_{max} (cm^{-3})	T_{32}^{ex} (K)	n_{min} (cm^{-3})	n_{max} (cm^{-3})
HD 313599	4.49±0.46	4.0±0.8	25	110	24.9±16.9	820	5420			
HD 70583	3.02±0.13	11.6±2.2	310	450	10.3±1.0	1090	1470			
HD 75149	0.59±0.05	3.1±0.4		35						
CD-46 4786	9.59±0.20	8.8±0.6	270	320	8.3±0.4	650	780			
HD 78344	14.59±0.15	10.9±0.4	350	380	7.1±0.2	470	520			
HD 75211	1.24±0.06	4.6±0.4	70	110						
NGC2024 IRS 1	25.29±2.44	15.5±13.0		670	15.0±4.9	1250	2910			
HD 229059	5.40±0.50	4.2±0.6	40	110	8.0±2.0	420	1220			
HD 29647	14.31±1.29	11.5±6.6	110	540	22.3±10.8	1510	4580	32.3±15.2	4240	17510
WR 105 (16.9 km s^{-1})	3.92±0.30	8.7±2.2	190	370	12.4±3.1	1090	2230	30.1±15.0	3350	16500
WR 105 (5.6 km s^{-1})	20.02±0.42	13.1±1.6	390	470	17.2±1.6	2250	2720	42.1±5.3	12850	17470
Cyg OB2 12* (6.7 km s^{-1})	8.71±0.45	7.3±1.0	210	300	9.9±1.3	940	1460			
Cyg OB2 12* (12.1 km s^{-1})	5.83±0.40	8.8±2.0	230	360	30.2±14.1	2320	5660			
HD 183143*	1.10±0.09	3.8±0.5	40	100						
WR 104*	9.49±0.22	9.7±1.0	320	400	8.7±0.5	870	1060	20.1±2.4	4530	6610
WR 118* (9.6 km s^{-1})	14.46±0.17	5.6±0.1	170	190	6.3±0.2	430	510			
WR 118* (41.2 km s^{-1})	18.61±0.18	7.3±0.2	250	260	10.1±0.2	1200	1290	14.0±0.6	2590	3130
WR 118* (56.6 km s^{-1})	3.17±0.15	8.4±1.3	240	360	10.9±1.4	1130	1670			
WR 118* (83.0 km s^{-1})	3.82±0.17				14.1±1.9	1640	2300	24.4±4.0	5680	9170

Note. — Column 2 is the total CO column density summed over all rotational levels. Level-specific CO column densities in sight lines marked with an asterisk were taken from Table 4 in McCall et al. (2002). The analysis outlined by Section 4 was used to calculate excitation temperatures, while Figure 5 was used to constrain $n(H_2)$.

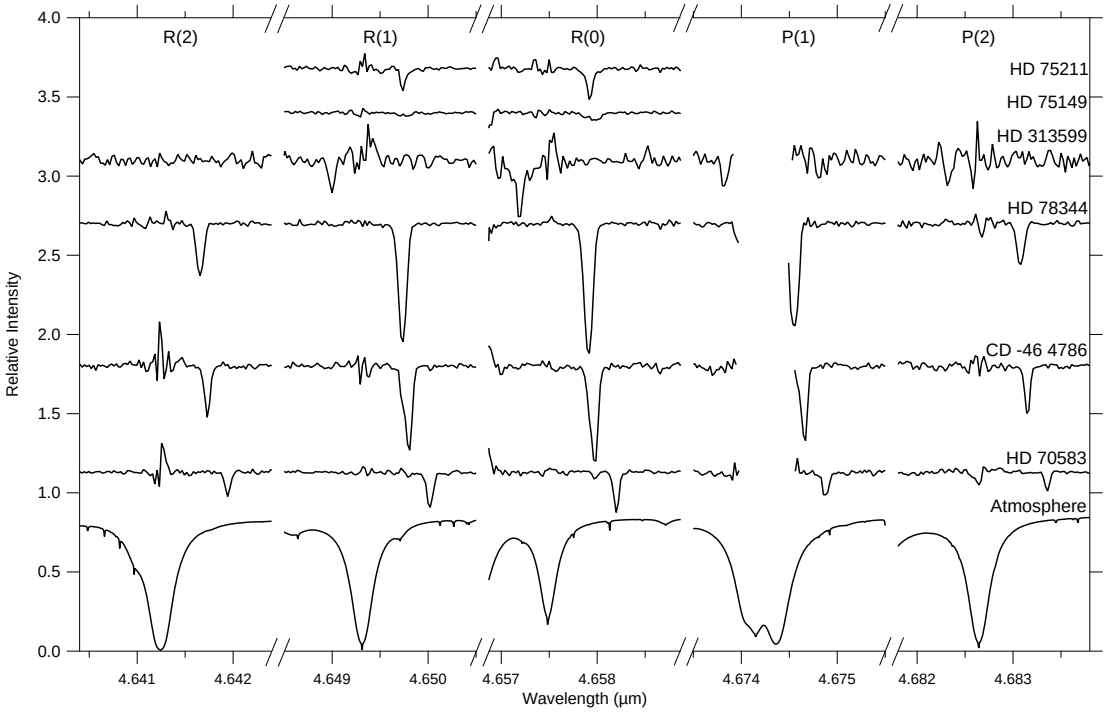

Figure 1. Fully reduced, normalized, and baseline corrected spectra (obtained using CRIRES at the VLT) with detected absorption features ranging from $R(2)$–$P(2)$. Portions of HD 75211 and HD 75149 were omitted because there were no detected transitions at those wavelengths. The noticeably noisy areas of each spectrum are due to imperfect removal of the atmospheric absorption features, which are shown in the spectrum at the bottom (Lord 1992). The missing portion of each spectrum near the $P(1)$ transition was removed, and spectra were shifted vertically for clarity.

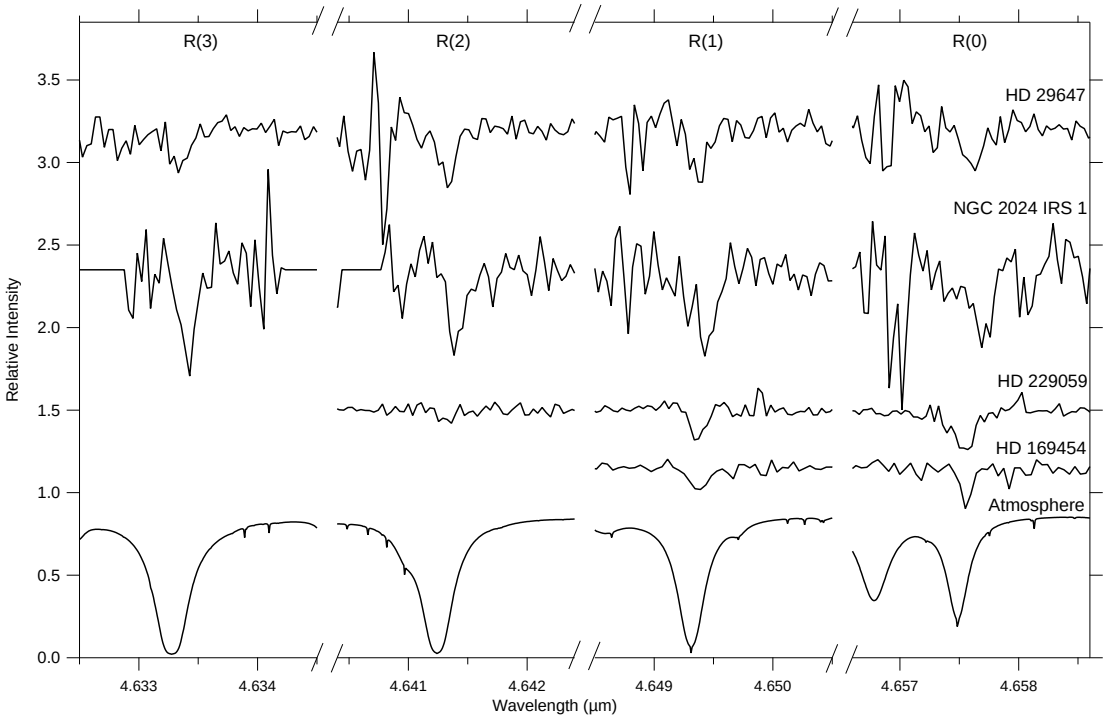

Figure 2. Fully reduced, normalized, and baseline corrected spectra (obtained using CSHELL at the IRTF and CGS4 at the UKIRT) with detected absorption features ranging from $R(3)$–$R(0)$ (shifted vertically for clarity). Portions of HD 229059 and HD 169454 were omitted because there were no detected transitions at those wavelengths. The atmospheric spectrum (Lord 1992) is shown at the bottom for comparison.

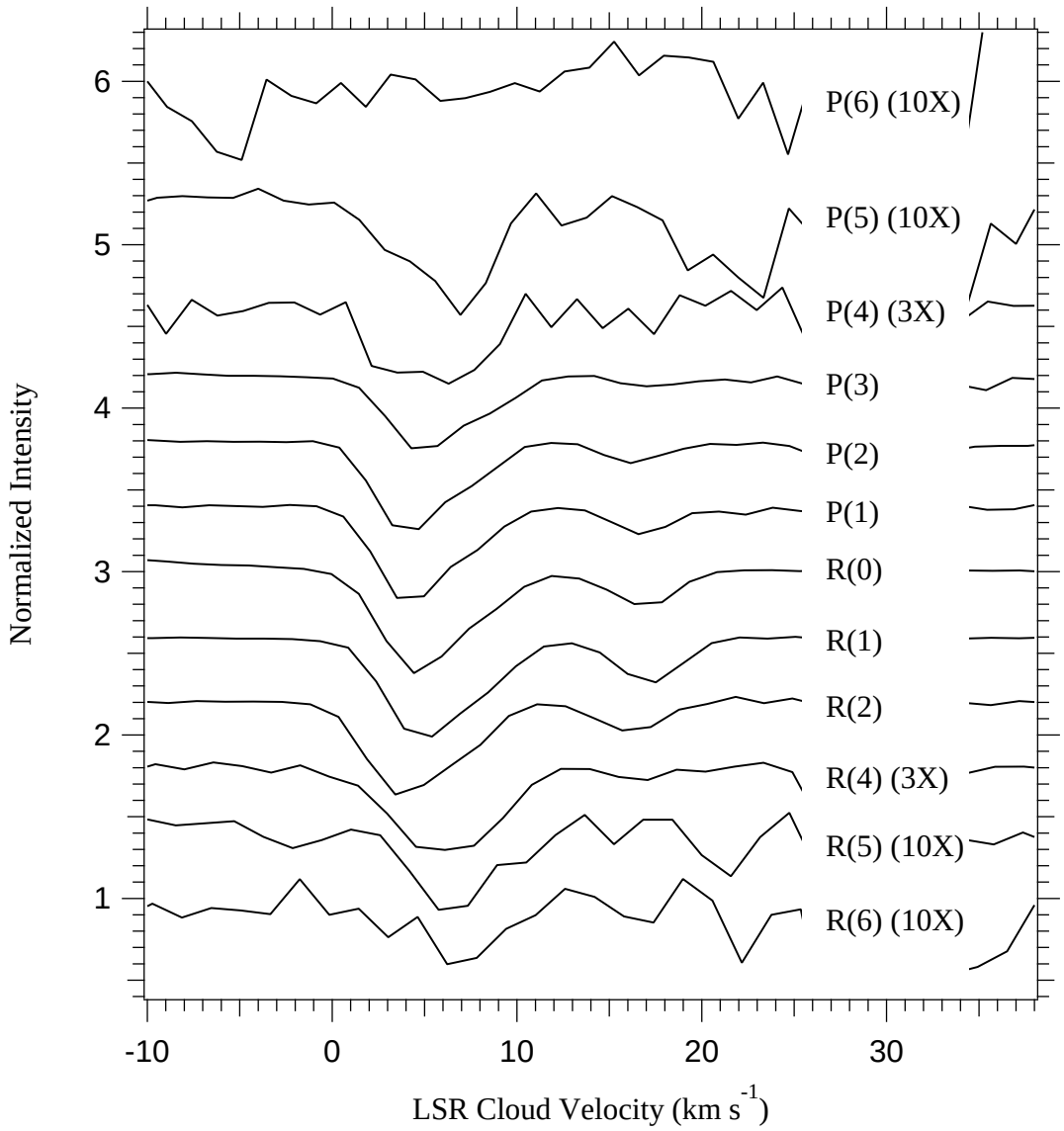

Figure 3. WR 105 plotted in velocity space (the portions of the spectrum containing the J = 4, 5, & 6 transitions are magnified for clarity). Its 2 velocity components can be easily seen at ∼5 km s^{-1} and ∼17 km s^{-1}. The noisy artifacts near 30 km s^{-1} were omitted due to imperfect removal of the atmospheric CO absorption line.

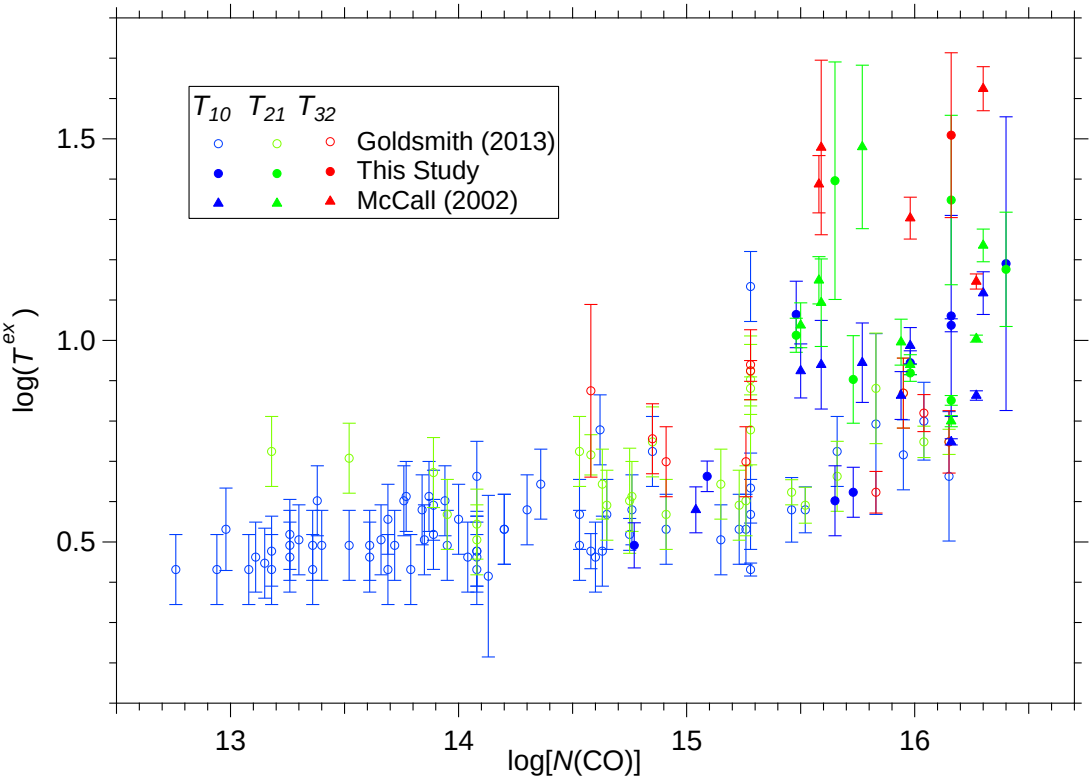

Figure 4. Excitation temperatures as a function of total CO column densities, along with calculated uncertainties in T^{ex}. The data from Goldsmith (2013) were taken from Sonnentrucker et al. (2007) and Sheffer et al. (2008), which targeted UV electronic transitions of CO, rather than the IR transitions we've observed. T^{ex} increases with N(CO).

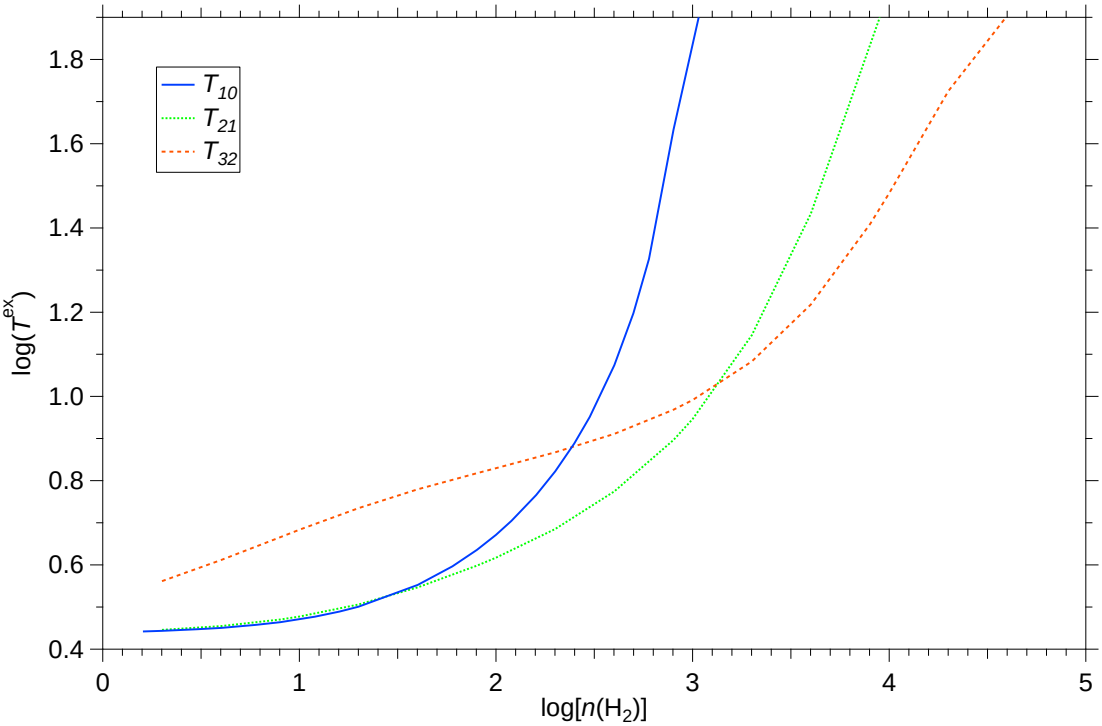

Figure 5. Excitation temperatures of CO calculated as a function of H_2 density through the Radex radiative transfer model (van der Tak et al. 2007). The model assumes optically thin transitions and a kinetic temperature of T_k = 100 K, which is roughly the average temperature of diffuse molecular clouds (Savage et al. 1977). Using calculated values of T^{ex}, we interpolate the density model to estimate the density of H_2 in each region.

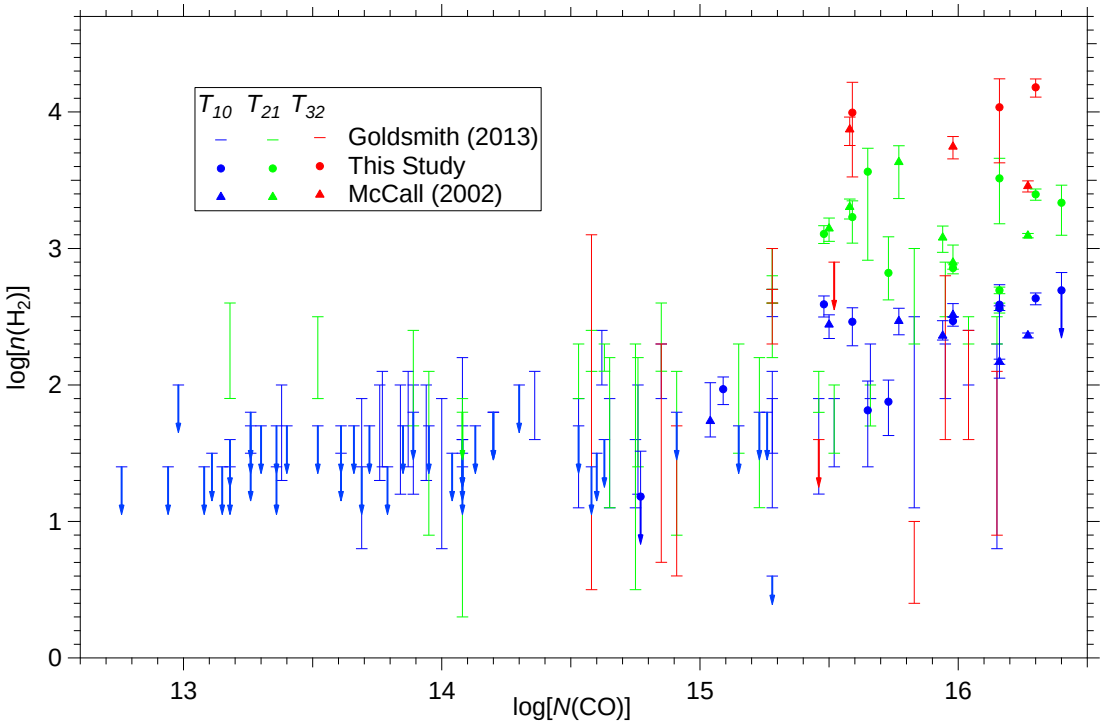

Figure 6. H_2 density as a function of CO column density with error estimates from Goldsmith (2013), McCall et al. (2002), and this study. The arrows denote values where only upper limits could be placed on density.